Published in final edited form as:
Magn Reson Med. 2014 March ; 71(3): 1336–1347. doi:10.1002/mrm.24744.

1.5 Tesla MRI-Conditional 12-lead ECG for MR Imaging and Intra-MR Intervention

Zion Tsz Ho Tse, PhD[1], **Charles L. Dumoulin, PhD**[2], **Gari D. Clifford, PhD**[3], **Jeff Schweitzer, MS**[4], **Lei Qin, PhD**[1], **Julien Oster, PhD**[3], **Michael Jerosch-Herold, PhD**[5], **Raymond Y. Kwong, MD**[5], **Gregory Michaud, MD**[5], **William G. Stevenson, MD**[5], and **Ehud J. Schmidt, PhD**[1]

[1]Radiology, Brigham and Women's Hospital, Boston, MA

[2]Radiology, Cincinnati Children's Hospital Medical Center, Cincinnati, OH

[3]Department of Engineering Science, University of Oxford, Oxford, UK

[4]Cardiovascular & Ablation Technologies, St. Jude Medical Inc, Minnesota, MN

[5]Cardiology, Brigham and Women's Hospital, Boston, MA

Abstract

Propose—High-fidelity 12-lead Electrocardiogram (ECG) is important for physiological monitoring of patients during MR-guided intervention and cardiac MR imaging. Issues in obtaining non-corrupted ECGs inside MRI include a superimposed Magneto-Hydro-Dynamic (MHD) voltage, gradient-switching induced-voltages, and radiofrequency (RF) heating. These problems increase with magnetic field. We intended to develop and clinically validate a 1.5T MRI-conditional 12-lead ECG system.

Methods—The system was constructed, including transmission-lines to reduce radio-frequency induction, and switching-circuits to remove induced voltages. Adaptive filters, trained by 12-lead measurements outside MRI and in two orientations inside MRI, were used to remove MHD. The system was tested on ten (one exercising) volunteers and four arrhythmia patients.

Results—Switching circuits removed most imaging-induced voltages (residual noise <3% of the R-wave). MHD removal provided intra-MRI ECGs that varied by <3.8% from those outside the MRI, preserving the true ST segment. In premature-ventricular-contraction (PVC) patients, clean ECGs separated PVC and sinus-rhythm beats. Measured heating was $<1.5\ C^0$. The system reliably acquired multiphase (SSFP) wall-motion-cine and phase-contrast-cine scans, including in subjects where 4-lead gating failed. The system required a minimum TR of 4ms to allow robust ECG processing.

Conclusion—High-fidelity intra-MRI 12-lead ECG is possible.

Keywords

ECG; Magneto-Hydro-Dynamic effect; Cardiac MRI; MRI-guided interventions

---

Corresponding Author: Zion Tsz Ho Tse, PhD: ziontse@uga.edu, Radiology, Brigham and Womens' Hospital, Room 74B, LMRC, 221 Longwood Ave, Boston, MA 02115.

Introduction

The 12-lead electrocardiogram (ECG) is a standard of care for cardiac physiological monitoring (1), and may be required during intervention on cardiac patients(2,3). In Cardiac Magnetic Resonance (CMR) imaging, where imaging is synchronized to the heartbeat, obtaining accurate single- or multiple-cardiac-phase MRI images depends largely on the reliability of the ECG gating (3,4). The three main obstacles to acquiring undistorted ECG signals within MR scanners are: superimposed Magneto-Hydro-Dynamic (MHD) voltages in the MR static magnetic field (B_0) (2), gradient- and body-coil-decoupling- switching induced voltages during imaging (5), and potential heating during radio-frequency (RF) transmission at the ECG electrodes, which can cause skin burns (6,7). If a conventional 12-lead ECG system is used inside an MRI, these three effects result in ECG traces that are frequently unreadable, may possess spectral peaks that are higher than the R-wave, and can potentially cause surface burns. These issues are larger when the MRI sequences employ fast rising and larger peak gradients, as the magnetic field increases, and when the RF amplifiers deliver more power.

In order to allow for cardiac imaging, MRI scanner manufacturers and several third-party vendors currently provide *3-4 lead MRI-conditional ECG systems*. These utilize MRI-conditional ECG electrodes, such as Quadtrode® from Invivo Inc., which are placed at small inter-electrode distances of 5-10cm, and use high-impedance (50-100 kOhm) lead wires. By placing the leads in close proximity, and using high-impedance leads, RF and gradient induction into the body and the ECG leads is reduced. However, relative to conventional 12-lead ECGs, this circuitry reduces the peak-to-peak ECG voltages by >50% (1), and increases the noise floor. Furthermore, low-pass (<30-50 Hz) filtering of the ECG signals, performed in the 4-lead ECG receivers to reduce this noise, leads to low-fidelity waveforms, so that current intra-MRI 4-lead ECGs are primarily applicable to acquisition synchronization, and not for physiological monitoring (1).

Gradient-ramp-induced and body-coil-decoupling-induced voltages have components within the ECG frequency band, so they are difficult to remove without affecting the true ECG, especially in high slew-rate sequences such as Steady State Free Precession (SSFP), which are frequently used in CMR imaging. The magnitude and spatial distribution of the electric fields induced by time-varying MRI gradients in the human body have been derived theoretically and demonstrated experimentally (8). Previous efforts (5,9-11) to reduce gradient noise have used adaptive filters, which receive as input the gradient patterns generated by the pulse sequence, and assume that the noise generated is linearly correlated to these patterns. This approach frequently fails since the linear relationship between gradient strength and the noise generated is not always valid.

When the Left Ventricle (LV) contracts, as shown in Fig. 1(a), blood is ejected from the LV and flows into the aortic arch, rapidly moving in a direction perpendicular to the B_0. Since blood is electrically conductive, an MHD voltage (V_{MHD}) arises according to the Lorentz's law. The V_{MHD} amplitude is frequently comparable to, or larger than, the R-wave peak in the ECG signal. This voltage is superimposed on the real ECG (ECG_{real}). V_{MHD} is dominant during the systolic S-wave-to-T-wave (S-T) segment (Fig. 1b, 1c)(12). ECG gating is affected when the triggering software erroneously triggers on MHD-peaks instead of the R-wave. Filtering out V_{MHD} using conventional filtering techniques is difficult, since its frequency spectrum and magnitude are similar to ECG_{real} (12,13).

"12-lead ECGs allow for rapid identification of heart disease, and are particularly important for detection of arrhythmia and acute ischemia (14). MRI-conditional 12-lead ECGs may enable MR-imaging and MRI-guided interventions of frequent arrhythmia patients, arising improvements in patient monitoring and image quality through the use of the gained ECG information to distinguish between different forms of cardiac conduction. Recent studies have both highlighted the great potential, and demonstrated the capabilities of MRI-guided cardiovascular electrophysiology (15-17), which is typical situation where MRI-conditional 12-lead ECGs would be indispensable for patient physiology monitoring during the procedure. This paper presents a 1.5 T MRI-conditional 12-lead ECG system, which attempts to extract intra-MRI ECGs free of V_{MHD} and imaging-induced voltages. "

Methods

12-lead ECG MRI-conditional Acquisition system Overall Design

The ECG acquisition and processing systems were designed to be compatible with standard cardiac imaging sequences, and the gating hardware available on commercial MRI scanners. As such, the system independently acquired and processed ECG data, and then sent clean ECG traces to the scanner's gating system for cardiac scan synchronization.

System hardware (Fig. 2a) comprised elements inside and outside of the scanner room. Inside the room, 10 MRI-conditional ECG electrodes (Quadtrode, Invivo, Gainesville, FL) were placed on a subject at conventional 12-lead torso positions. 50-Ohm-impedance coaxial cables (COAX) equipped with carbon-fiber ECG-clips conducted the ECG voltages from the electrodes to the scanner-room's penetration panel, where the signals were conducted out via RF low-pass (LP) filters. High-voltage 0.22 mFarad DC-blocking capacitors (ATC, Huntington Station, NY) were placed between the LP filter's high-pass path and the penetration-panel ground (Fig. 2d), in order to provide patient electrical isolation. The capacitors blocked low-frequency (0-100 Hz) currents from going to the ground, while allowing the high-frequency (>1.9 MHz) filtered signals to pass through, satisfying the high-pot and leakage-currents requirements for medical equipment (18). After exiting the room, ECG signals passed through the gradient-RF Blanking hardware, which is described below, designed to filter out Gradient and RF noise, before being recorded on a Cardiolab-IT (GE, Waukesha, WI) digital ECG-recording system. The Cardiolab ECG amplifier was placed outside the scanner room to prevent its generating RF noise inside the scanner room.

For further software processing (Fig. 2a), ECG traces were streamed out from a Digital-to-Analog (D/A) port in Cardiolab to a 64-bit real-time processing station, which read the data via two multi-I/O cards (National Instruments, Austin, TX). The extracted clean ECG signals, along with the estimated SV traces, were displayed on the graphic user interface of the processing station, as well as on in-room MRI-conditional displays. Scan triggers were also sent out from the processing station to the MRI scanner, allowing for prospective, or retrospective, cardiac-gated scans based on the user's desired beat-type, Sinus Rhythm, (SR), or Premature Ventricular Contraction (PVC) preference.

Suppression of Radiofrequency currents in ECG conduction lines

Heating at ECG electrodes, induced by the MRI's RF pulses, was a concern (6,19), since the 10 electrodes used in 12-lead ECG were placed at larger separations (up to 40 cm) than in the 4-lead design (<5 cm). The ECG cables can therefore act as improved antennas, potentially receiving more induced RF. In addition, a decision was made not to use high-impedance transmission-lines, since such lines reduce ECG fidelity (1). The goal was therefore to reduce the RF induction into these cables and to attenuate the propagation of residual induced RF.

The single-conductor ECG leads used in conventional ECG systems were replaced with mm-diameter COAX (Temp-Flex 50HCX-55, South Grafton, MA), in which the coaxial shield was connected to DC-blocking capacitors and thereafter to the scanner room's penetration panel at one end, and left open-circuited at the electrode end. The COAX center-conductor was connected to carbon ECG clips (Fig. 2b), and then to the ECG electrodes. The grounded small-diameter coaxial leads were intended to reduce induced RF currents inside the bore. In addition, radio-frequency ferrite chokes (FerriShield, Tampa, FL) were mounted at specific points on the ECG cables (Fig. 2c), once the cables were outside the MRI 5-gauss line.,. The ferrites were placed at positions where the 64-MHz interference was maximal, as determined by network analyzer measurements, which translated to distances of 140 cm, corresponding to coaxial-cable half-wavelengths (Fig. 2d). The ferrites' weight also reduced transmission line vibration.

shows A low-pass RF filtering circuit box (Fig. 2e) on the outside of the penetration panel contained Minicircuits (Brooklyn, NY) 1.9-MHz low-pass filters on each line, and connected between the ECG leads inside the scanner room and the Cardiolab ECG input, preventing RF-noise from propagating into the scanner room on the ECG lines.

Suppression of Gradient and High-Voltage noise induction onto ECG

When MR gradient pulses are applied, the changing magnetic fields induce currents in ECG cables and in dielectric substances within the patient body, whose amplitude can be several Volts. These voltages can saturate the ECG recording amplifier. Gradient-noise is difficult to address, because its amplitude is potentially much stronger than the ECG signals, and because the noise's magnitude, direction, frequency and duration - vary significantly, subject to the different imaging sequences used, and the imaging slice's position and orientation.

Large ECG disturbances also occur during RF pulse transmission, resulting from high electric fields created by high-voltage (15 KV) DC pulses sent to bias the body coil's diodes during RF pulse transmission ("RF unblanking"). These voltages begin ~100 μs before the RF pulse and last over its duration (1-2 ms) to ensure that the body coil is resonant during transmission. The electric fields created by these voltages induce noise at ECG frequencies. Rather than using software techniques, as previously attempted (9,11), a multi-fold hardware solution was implemented. To reduce current induction into the ECG cables, thin shielded COAX were used. To further suppress gradient-induced distortions, ECG signals were prevented from reaching the ECG amplifier both during the Gradient-Ramps and during the "RF unblanking" periods (GR&RF). The six components (Fig. 2g (1)-(6)) were:

1. Real-time waveform outputs of Gx, Gy and Gz (Fig. 2f) from the MRI gradient cabinet were processed using a custom-made gradient ramp detection circuit to generate $\mathrm{TTL}_{\mathrm{GR}}$ signals whenever a Gradient Ramp (GR) was detected.
2. The MRI RF cabinet output the waveform of the "RF unblanking" signal, a signal sent to the RF body coil in order to reverse bias the body coil's diodes during RF pulse transmission. A custom circuit then produced a $\mathrm{TTL}_{\mathrm{RF}}$ for the entire duration of this period (typically 1-2 msec).
3. To ensure that the receiver cut-off lasted beyond each GR&RF noise period, a variable-time extension of the TTL control was provided.
4. Both $\mathrm{TTL}_{\mathrm{GR}}$ and $\mathrm{TTL}_{\mathrm{RF}}$ were combined together using an OR switch, which is denoted as $\mathrm{TTL}_{\mathrm{GR\&RF}}$ in Fig. 2f.
5. $\mathrm{TTL}_{\mathrm{GR\&RF}}$ signal was sent to rapid Single-Pole-Double-Throw (SPDT) electronic switches (Analogic Devices, Norwood, MA), which disconnected the ECG signals from the Cardiolab amplifier, allowing the amplifier to acquire only ECG signals free from GR&RF induction. This switching circuitry utilized rapidly-responding (<200nsec) electronics, guaranteeing synchronization between the ECG acquisition system and the MRI gradient and RF amplifiers.
6. To ensure that the SPDT switches cut off the earliest occurrence of GR&RF noise, a 70-μsec delay line of the EGC signals was placed before the switches. This delay line was combined with a 25-KHz low-pass Bessel filter (TTE, Los Angeles, CA). Note that that this specific delay duration is required due to the signal timings originating in the GE (Waukesha, WI) 1.5 or 3T scanners, and other delay durations will be required for different scanners.

Processing system for Real-time ECG extraction

The real-time digital ECG signal processing steps, including MHD filtering, QRS complex detection and PVC/SR classification, were performed in an HP XW8600 multiple-processor workstation (Palo Alto, CA), which received the 12-lead ECG traces from Cardiolab.

The data-processing procedure (Fig. 3a) involved: (a) a pre-processing stage which included 200Hz low-pass filtering, low-frequency (0.5 Hz-zero phase, breathing related) baseline removal and de-noising, (b) a QRS complex and beat type detection stage, (c) an adaptive filtering stage for MHD-removal, and (d) a PVC or Sinus Rhythm beat-type selection stage.

The adaptive filtering procedure (c) was implemented in Matlab (Natick, MA) (Fig. 3a). It employed (c1) QRS complex detection, (c2) PVC/SR beat decoupling, (c3) separate PVC-beat and SR-beat adaptive filters to decouple the V_{MHD} from $\mathrm{ECG}_{\mathrm{real}}$, and (c4) ECG data recombination.

With data-processing complete, an ECG-gating circuitry, operated via a Digital-to-Analog (D/A) card in the processing workstation, sent gating triggers to the MRI scanner, based on the extracted clean ECGs.

MHD-filtering procedure

For V_{MHD} removal, Least Mean Squares (LMS) Finite Impulse Response (FIR) adaptive filtering was implemented (20). The LMS FIR adaptive filter was chosen due to its simple implementation and fast filter coefficient optimization based on the stochastic gradient algorithm (20). This filter is characterized by two parameters: (i) the FIR filter length n, the number of filter coefficients required to adapt to the principal features of the patient's MHD signal in the acquired ECGs, and (ii) the step size μ, determining the filter convergence speed and stability. n and μ were chosen to be 10 and 0.0015, respectively, which achieved stable ECG outputs and short filter adaptation times.

Fig. 3b shows the formulation of the adaptive MHD filtering. An unknown patient-dependent MHD voltage was modeled by an MHD adaptive filter model, which first learned the MHD signal characteristics during an initial ECG learning phase, and then processed the measured signal $ECG_{measured}$ in order to remove V_{MHD} and derive ECG_{real}.

The derived ECG_{real} was then fed back into the MHD adaptive filter model to adjust the filter's transfer functions to approximate the cardiac-vascular MHD mechanism. Since the MHD voltage was mainly generated by blood flow through the aortic arch, the time-integrated systolic MHD voltage, $\int \mathrm{V}_{MHD}(t)\,dt$, was used to estimate the beat-to-beat Stroke Volume(13,21).

The learning phase was performed to train the filters to detect the MHD signal characteristics. Three sets of 20-sec breath-held ECGs were acquired for training. Fig. 3c shows 12-lead ECG measurements with subjects placed in three positions (i), (ii), and (iii), during 20-sec breath holds.

In position (i), the patient was placed outside the MR:

$$ECG_{\mathrm{i}}=ECG_{\mathrm{real}} \quad (1)$$

In position (ii), the patient was placed inside the magnet:

$$ECG_{ii}=ECG_{\mathrm{real}}+\mathrm{V}_{MHD} \quad (2)$$

In position (iii) patient orientation was reversed (i.e. feet first vs. head first) inside the magnet:

$$ECG_{iii}=ECG_{\mathrm{real}}-\mathrm{V}_{MHD} \quad (3)$$

Each of the three sets of ECG signals received a preliminary set of signal processing stages, including baseline removal, denoising and 3D-QRS complex detection. An R-R cycle-length normalization to 60 Beats per Minute (BPM) was applied, since the subjects' heart rates frequently varied between the three (above) scans, and algebraic manipulation of the three sets needed to be performed in order to provide initial estimates of ECG_{real} and V_{MHD}, as explained below.

During training, ECG measurements (i) and (ii), or (i) and (iii), were applied for adaptive filter training, subject to the patient orientation subsequently utilized for imaging. As V_{MHD} in each ECG channel can be derived from equations (1-3), the third set of ECG measurements was used to further verify the software and hardware setup, since the magnitude of V_{MHD} for orientations (ii) and (iii) was approximately the same in each ECG channel, but with reversed polarity. After the training period, the adaptive filters had their transfer function self-adjusted for newly acquired ECG signals, according to the LMS optimization algorithm (20).

Once the adaptive filters converged, the learning phase was complete, and the filtering software was ready to separate ECG_{real} from V_{MHD} in real-time during subsequent ECG recording inside the MRI.

Real-Time processing method

The processing code was linked to LabView (National Instruments, Austin, TX) software, which also provided a graphic display and user interface.

The processing framework (Fig.3a-b), filled a 25-ms temporal sliding-window buffer with 2-Khz sampling rate real-time ECG traces from all leads. The sliding window was updated whenever a new time point was acquired.

In the pre-processing stage, a third-order zero-phase band-pass (0.5Hz high-pass, 150Hz low-pass) filter, was used, followed by a third-degree polynomial Savitzky-Golay denoising(22).

For MHD adaptive filtering, a sliding window buffer containing 2-seconds of ECG data was formed, and both its R-R intervals and the ECG training data were aligned to 60 BPM to develop a time-domain relationship between the ECG training data acquired outside the MRI and the recently-acquired intra-MRI ECG traces. LMS-FIR adaptive filtering (Matlab *ADAPTFILT.LMS*) was then applied separately for the SR beats, and for the PVC beats, in the sliding window, deriving ECG_{real} from V_{MHD} for both beat types. The derived signals were then aligned back with their original heart rates, stored in the computer, and then sent to the LabView display and the user Interface.

Phantom and Swine model for RF heating testing

ASTM F2182-02a standard was initially used to investigate RF heating effects by the MRI scanner (6). This phantom was also used to initially assess the interference between MRI imaging and the 12-lead system.

A large adult swine weighing 60kg was then used to perform electrode heating measurements, under an approved institutional IACUC protocol. The swine skin was shaved to remove all hair. Temperature was measured using Luxtron (Stockholm, Sweden) fiber-optic probes placed between the ECG electrodes and the skin. The 10 electrodes were placed at 12-lead-ECG chest locations on this swine, considered to be a reliable model to simulate human-subject SAR effects since the distance between the electrodes, as well as the skin conditioning, were similar to a shaved human subject, with the swine's delicate skin allowing even slight burns to be observed. The swine was continuously scanned for 30 minutes in a 1.5T MRI scanner, using MRI sequences at the FDA's maximal allowed specific absorption rate (4 W/kg) and the maximal allowed magnetic field temporal change (20 T/s).

Patient and normal subjects

12-lead ECGs were acquired, inside a GE 1.5 T MRI scanner, in 10 healthy volunteers and four patients; two with chronic Atrial Fibrillation (AF) and two with severe Idiopathic Outflow Tract Premature Ventricular Contractions (IOT PVCs), under an approved institutional IRB. The two AF patients were 70 and 49 year-old males referred for assessment of left-atrial anatomy prior to catheter-based isolation of the pulmonary veins. The IOT PVC patients were a 63 year-old female with a history of a non-ischemic cardio-myopathy, and heart failure, with high-grade ventricular ectopy and AF, referred for assessment of infiltrative cardio-myopathy, and a 50 year-old female patient with right ventricular ectopy.

In one athletic volunteer, we studied MHD changes with heart rate by performing an exercise in which a rubber-band (Golds Gym Resistance Tube Kit) was stretched between the subject's hands and feet inside the bore. The chest in all male subjects was shaved to ensure good ECG signal conductivity between ECG electrodes and the chest skin.

Cardiac MR imaging was performed after completion of the swine heating tests, using an approved institutional IRB, on five volunteers and two IOT-PVC patients, with the 10 ECG leads placed underneath an 8-channel cardiac array coil. Imaging sequences included 2D gradient-echo (GRE), 2D fast spin echo and 2D steady-state-free-precession (SSFP) multiphase wall-motion. Repetition times (TRs) from 2-2000 msec were tested. Interference between the MRI and the ECG system was assessed by comparing the SNR of non-gated FSE, GRE, and SSFP images acquired without and with the 12-lead system connected to the subject's skin.

Acute Ischemia detection in swine

To validate 12-lead ECG functionality in detecting acute ischemia inside the MRI, a swine study was performed to study S-wave to T-wave (ST) ECG elevation. A 2-mm diameter coronary balloon catheter filled with Gadolinium-doped water was inserted into the swine's distal Left Anterior Descending (LAD) under X-ray guidance. The swine was moved to a GE 1.5T MRI suite where continuous 12-lead ECG monitoring (Fig.9a) and multiphase wall imaging (Fig.9(b-d)) were performed. Acute ischemia was produced by inflating the balloon inside the MRI suite. Concurrent cardiac cine imaging was performed from before the occlusion to the swine's death.

At t=0 seconds, the balloon was inflated to 20 atmospheres. Cine MRI and simultaneous ECG monitoring were performed until death occurred some 20 minutes later. The balloon's position was confirmed using post-mortem 3D T1 imaging, and T2 imaging was used to detect edema.

Results

Removal of gradient and RF noise from ECG traces

Fig. 4 shows ECG results for gradient noise removal during imaging in a volunteer, verifying the proper function of the GR&RF circuit. GR&RF induced noise (Fig. 4(d)) was reduced to ±0.05mV, equivalent to 2.8% of the R-wave amplitude, for most CMR sequences. Since each blocked interval was short (0.5-2ms) with respect to the repetition time (TR), the resulting ECG waveform distortion was minor. The ECG amplitude was reduced proportionately to the duration of the blocking time, so the correct amplitude was restored using a variable digital amplifier. A minimum TR of 4 ms was required to allow sufficient flat-top time for ECG recording, which prohibited the use of shorter TR GRE and SSFP sequences.

Real ECG extraction and MHD physiology

ECG extraction in the presence of MHD noise was tested on all 14 subjects. Fig. 5 shows processing of an IOT PVC patients' V6 channel with monomorphic ventricular bigeminus. The results (Fig. 5a-d) demonstrate separation of ECG_{real} (Fig. 5b) and V_{MHD} (Fig. 5c), with the S-T segment well preserved. The complete 12-lead ECG obtained from this patient outside the MRI is shown in the supplement. From Fig. 5c, V_{MHD} peaks during the S-T segment, and is smaller during the PVC beats relative to SR beats. SV estimation (Fig. 5d), using the systolic-integrated V_{MHD}, suggested that these IOT PVC beats produced a lower SV than during SR, which is consistent with previous data (23,24). Statistical analysis of S-T segment preservation (Fig. 5e-g) clearly demonstrates the degree to which MHD removal restores the S-T segment amplitude to their true (outside the MRI) value.

Fig. 6a-d shows processing of an AF patients' V6 channel. The AF patient results (Fig. 6a-d) showed an irregular V_{MHD} (Fig. 6c) and SV (Fig. 6d), which can be explained by ventricular-filling differences at the widely varying heart rates (100-150 BPM). The AF results demonstrate that the adaptive MHD filter converges in 1-2 cardiac cycles, even with patient heart-rate changes of >20 BPM.

Fig. 6e-g shows processing of an exercising athlete's V6 channel. The V_{MHD} filtering procedure was able to adapt to gradual heart-rate changes from 44 BPM to 87 BPM that occurred when the athlete exercised inside the scanner, with his stroke volume (Fig. 6g) continuously monitored by the time-integrated systolic V_{MHD}. V_{MHD} increased with heart rate (Fig.6f), suggesting that a higher stroke volume (Fig. 6g), was required during exercise. Additionally, the extracted MHD signals exhibited greater variability at the higher heart rates (Fig. 6f), which may be explained by greater turbulent flow in the aortic arch at higher blood flow rates.

To evaluate the accuracy of the adaptive filters over time, ECGs were measured in subjects at intervals of 5, 10 and 15 minutes, inside and outside the magnet. The processed ECG_{real} acquired inside the magnet was compared with ECG data acquired outside the magnet for validation. Fig. 7 and Table 1 show the cross-correlation-index and fitting normalized-RMS-error results in 10 volunteers and 4 patients.

The average cross-correlation index was 96.2% and 94.1% in healthy and patient subjects, respectively, and the average RMS error normalized by the R-wave peak was 2.6% and 2.4%, respectively. The ECG traces from the exercising athlete were particularly challenging to the MHD filtering procedure, and had the lowest cross correlation index (92.3%) and the highest RMS error (3.8%). This can be explained by rapid changes in SV and V_{MHD} that occurred in the ECG traces, resulting in a relatively longer adaptation time of 4 cardiac cycles (2.8 sec), instead of the 2-cardiac-cycle average for the other subjects.

MRI-safety and compatibility RF Heating

The swine imaging experiment showed less than 1.5 C^0 heating measured at any of the ECG electrodes or patient-end of the ECG cables in the strongest MRI pulse sequences. The system was subsequently used in four human subjects during maximal SAR imaging, and no electrode heating was reported. No surface burns or irritation were observed.

MR Imaging and ECG Interference

Interference between the ECG system and the scanner’s image quality was studied on both phantoms and human subjects. Less than 5% image Signal-to-Noise-ratio (SNR) reduction was observed with all the imaging sequences utilized. Similarly, noise appearing at the ECG traces, caused by switched gradients, was quantified during maximal slew-rate imaging sequences, including SSFP, with results showing less than 0.05mV peak-to-peak noise on the ECG signals (Fig. 4d).

1.5T CMR Imaging was performed using the 12-lead ECG system on two volunteers and in two patients (Fig. 8), including a subject with very high V_{MHD}, where the conventional 4-lead ECG did not properly trigger during cardiac imaging. ECG traces were acquired and processed in real-time, and the highest-voltage traces sent to the scanner’s gating circuitry. Fig. 8c shows 30 frames-per-second retrospective ECG-gated SSFP results of the subject where 4-lead ECG failed due to the strong V_{MHD} peak. Gating quality was consistently good, since the R-wave peaks were clearly dominant, and the dispatched ECG voltage (5 mV) was close to the maximal triggering voltage accepted by the scanner. Since beats were not missed, breath-hold scans were completed in the prescribed scan duration, and blurring was not observed.

Swine Acute Ischemia detection with concurrent MRI

After occluding the swine LAD, S-T elevation was detected 1.5 seconds later (Fig. 9(a2)) with the 12-lead system, progressing to acute ischemia (Fig. 9(a3-4)), bradycardia and to death 20 minutes later. Left and right ventricular dysfunction and unusual flow vortexes were visualized with serial cine MRI during this entire period (Fig. 9(c1-4)). Epicardial edema was observed proximal to the balloon’s position in the post-mortem T2 images (Fig. 9d). The MR-compatible 12-lead ECG detected acute ischemia, while the simultaneous MRI imaging visualized the progression of LV and RV dysfunction.

Discussion

12-lead MRI-conditional ECG acquisition and processing systems were developed and tested in ten healthy volunteers and four patients in a 1.5T scanner. RF and gradient interference was suppressed using a hardware signal-blocking circuit, as well as a set of measures that were taken to reduce electromagnetic interference between the ECG equipment and the MRI scanner. Results showed that ECG trace noise was less than 0.05mV PTP, MRI SNR reduction was <5% and patient heating was not reported. An adaptive ECG signal filtering procedure, implemented on a multiprocessor workstation, removed the MHD voltage from intra-MRI ECG signals. MHD-removal utilized three sets of ECG measurements to train adaptive FIR filters. Quantitative MHD removal was extensively tested during breath-holds, and some modifications may be required for its implementation during free-breathing.

Swine validation demonstrated the functionality of the proposed 12-lead ECG system to rapidly detect acute ischemia. Use of the system can therefore reduce the risks associated with intervention on patients with ischemic histories. Since ischemia was produced inside the MRI, it was also possible to study the progression of ventricular dysfunction, which may have consequences for basic science and for resuscitation science.

Reliable ECGs in SSFP and GRE with TR<4ms were not obtained, because the blanking periods, 80-90% of the TR, did not leave sufficient intervals for ECG recording. This is currently an important limitation, since short TR is used extensively in cardiac MRI. We believe that it may be possible to provide accurate ECGs during such sequences if blanking is not performed during all gradient ramps, such as, for example, during the phase-encoding blips, since extremely short gradient waveforms produce low-intensity noise which is spread over a wide frequency band.

The innovations originating from this study may also extend the use of 3T cardiac MRI, where RF patient heating is a greater risk and MHD voltages are twice those at 1.5T. MHD processing may enable the non-invasive estimation of beat-to-beat SV, which currently requires invasive TEE, or dedicated cardiac MRI scans. A larger subject study is required to verify and better quantify this method, but it may provide a means to monitor subject well-being during an MRI-guided intervention.

The intra-MRI ECG monitoring system may permit MRI studies of severely ill patients, such as sedated patients, those after stroke and post-infarction, as well as additional patient populations that require on-line ECG monitoring, and are therefore presently excluded from MR imaging or MRI-guided interventions.

Supplementary Material

Refer to Web version on PubMed Central for supplementary material.

Acknowledgments

This work was supported by AHA 10SDG261039, NIH U41-RR019703, a BWH BRREF award, and a Hong-Kong Croucher fellowship.

References

1. Kligfield P, Gettes LS, Bailey JJ, Childers R, Deal BJ, Hancock EW, van Herpen G, Kors JA, Macfarlane P, Mirvis DM, Pahlm O, Rautaharju P, Wagner GS. Recommendations for the standardization and interpretation of the electrocardiogram: Part I: The electrocardiogram and its technology: A Scientific Statement from the American Heart Association Electrocardiography and Arrhythmias Committee, Council on Clinical Cardiology; the American College of Cardiology Foundation; and the Heart Rhythm Society. Endorsed by the International Society for Computerized Electrocardiology. Heart rhythm: the official journal of the Heart Rhythm Society. 2007; 4(3):394–412. [PubMed: 17341413]
2. Kangarlu A, Burgess RE, Zhu H, Nakayama T, Hamlin RL, Abduljalil AM, Robitaille PML. Cognitive, cardiac, and physiological safety studies in ultra high field magnetic resonance imaging. Magnetic resonance imaging. 1999; 17(10):1407–1416. [PubMed: 10609989]
3. Dimich RN, Hedlund LW, Herfkens RJ, Fram EK, Utz J. Optimizing Electrocardiograph Electrode Placement for Cardiac-Gated Magnetic Resonance Imaging. Investigative Radiology. 1987; 22(1): 17–22. [PubMed: 3818232]
4. Fischer SE, Wickline SA, Lorenz CH. Novel real-time R-wave detection algorithm based on the vectorcardiogram for accurate gated magnetic resonance acquisitions. Magnetic Resonance in Medicine. 1999; 42(2):361–370. [PubMed: 10440961]
5. Abächerli R, Pasquier C, Odille F, Kraemer M, Schmid JJ, Felblinger J. Suppression of MR gradient artefacts on electrophysiological signals based on an adaptive real-time filter with LMS coefficient updates. Magnetic Resonance Materials in Physics, Biology and Medicine. 2005; 18(1):41–50.
6. ASTM-F2182. Standard Test Method for Measurement of Radio Frequency Induced Heating On or Near Passive Implants During Magnetic Resonance Imaging. American Society for Testing and Materials. 2011
7. Schaefers G. Testing MR Safety and Compatibility. Engineering in Medicine and Biology Magazine, IEEE. 2008; 27(3):23–27.
8. Bencsik M, Bowtell R, Bowley R. Electric fields induced in the human body by time-varying magnetic field gradients in MRI: numerical calculations and correlation analysis. Physics in medicine and biology. 2007; 52(9):2337–2346. [PubMed: 17440238]
9. Odille F, Pasquier C, Abacherli R, Vuissoz PA, Zientara GP, Felblinger J. Noise Cancellation Signal Processing Method and Computer System for Improved Real-Time Electrocardiogram Artifact Correction During MRI Data Acquisition. Biomedical Engineering, IEEE Transactions on. 2007; 54(4):630–640.
10. Oster J, Pietquin O, Kraemer M, Felblinger J. Nonlinear Bayesian Filtering for Denoising of Electrocardiograms Acquired in a Magnetic Resonance Environment. Biomedical Engineering, IEEE Transactions on. 2010; 57(7):1628–1638.
11. Oster J, Pietquin O, Abächerli R, Kraemer M, Felblinger J. Independent component analysis-based artefact reduction: application to the electrocardiogram for improved magnetic resonance imaging triggering. Physiological Measurement. 2009; 30:1381–1397. [PubMed: 19887719]
12. Gupta A, Weeks AR, Richie SM. Simulation of Elevated T-Waves of an ECG Inside a Static Magnetic Field (MRI). Biomedical Engineering, IEEE Transactions on. 2008; 55(7):1890–1896.
13. Nijm G, Swiryn S, Larson A, Sahakian A. Extraction of the magnetohydrodynamic blood flow potential from the surface electrocardiogram in magnetic resonance imaging. Medical and Biological Engineering and Computing. 2008; 46(7):729–733. [PubMed: 18239947]
14. Dubin, D. Rapid interpretation of EKG's. Cover Publishing Company; 200
15. Weiss S, Wirtz D, David B, Krueger S, Lips O, Caulfield D, Pedersen SF, Bostock J, Razavi R, Schaeffter T. In vivo evaluation and proof of radiofrequency safety of a novel diagnostic MR electrophysiology catheter. Magnetic Resonance in Medicine. 2011; 65(3):770–777. [PubMed: 21337409]
16. Nordbeck P, Bauer WR, Fidler F, Warmuth M, Hiller KH, Nahrendorf M, Maxfield M, Wurtz S, Geistert W, Broscheit J. Feasibility of Real-Time MRI With a Novel Carbon Catheter for Interventional Electrophysiology. Circulation: Arrhythmia and Electrophysiology. 2009; 2(3):258–267. [PubMed: 19808476]

17. Sommer P, Grothoff M, Eitel C, Gaspar T, Piorkowski C, Gutberlet M, Hindricks G. Feasibility of real-time magnetic resonance imaging-guided electrophysiology studies in humans. Europace. 2012 doi: 10.1093/europace/eus230.
18. IEC-60601. Medical equipment and medical electrical equipment. International Electrotechnical Commission; 2012.
19. Woods TO. Standards for medical devices in MRI: Present and future. Journal of Magnetic Resonance Imaging. 2007; 26(5):1186–1189. [PubMed: 17969160]
20. Ingle, V.; Proakis, J. Digital Signal Processing using Matlab. Thomson; 2007.
21. Kinouchi Y, Yamaguchi H, Tenforde TS. Theoretical analysis of magnetic field interactions with aortic blood flow. Bioelectromagnetics. 1996; 17(1):21–32. [PubMed: 8742752]
22. Savitzky A, Golay MJE. Smoothing and Differentiation of Data by Simplified Least Squares Procedures. Analytical Chemistry. 1964; 36(8):1627–1639.
23. McKay R, Spears J, Aroesty J, Baim D, Royal H, Heller G, Lincoln W, Salo R, Braunwald E, Grossman W. Instantaneous measurement of left and right ventricular stroke volume and pressure-volume relationships with an impedance catheter. Circulation. 1984; 69(4):703–710. [PubMed: 6697458]
24. Voss A, Baier V, Schumann A, Hasart A, Reinsperger F, Schirdewan A, Osterziel K-J, Leder U. Postextrasystolic regulation patterns of blood pressure and heart rate in patients with idiopathic dilated cardiomyopathy. The Journal of Physiology. 2002; 538(1):271–278. [PubMed: 11773334]

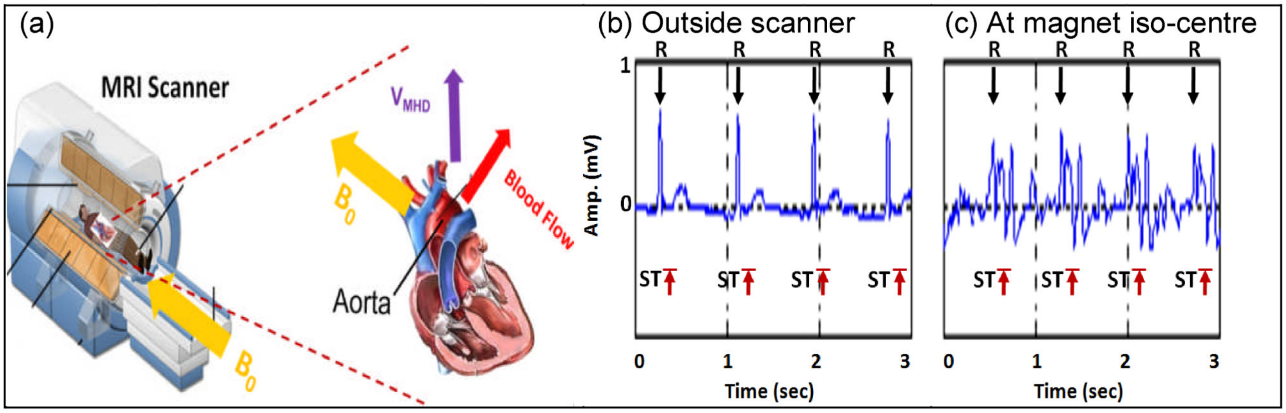

Fig.1.

(a) V_{MHD} (purple) induced during blood flow (red) perpendicular to B_0 (yellow) in the aortic arch. Human subject's V2 channel ECG; (b) outside MRI and (c) distorted by V_{MHD}, peaking during S-T segment inside a 1.5T MRI.

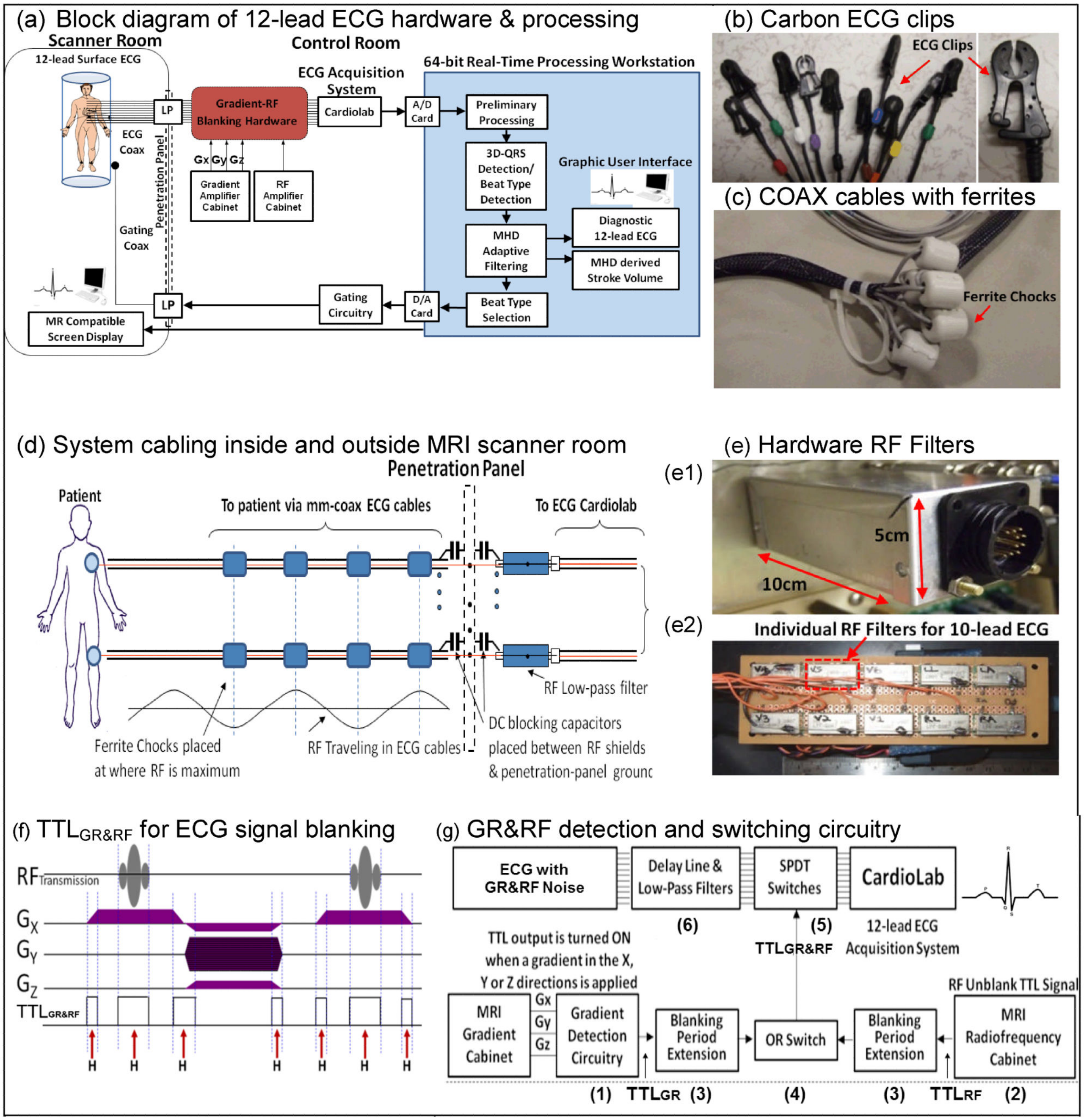

Fig.2.

(a) System diagram. (b) Carbon ECG clips. (c) ECG cables with ferrites. (d) Cabling: Ferrites were placed at points with maximal RF wave amplitude to attenuate propagation. (e) RF low-pass filters (e1-exterior, e2-interior) for ECG cables during passage through the penetration panel. (f) $\mathrm{TTL}_{\mathrm{GR\&RF}}$ pulses (H symbols with red arrows) generated during GR&RF periods in an exemplary MRI sequence. (g) GR&RF switching circuit diagram. Components (1)-(6) are shown and explained in the text.

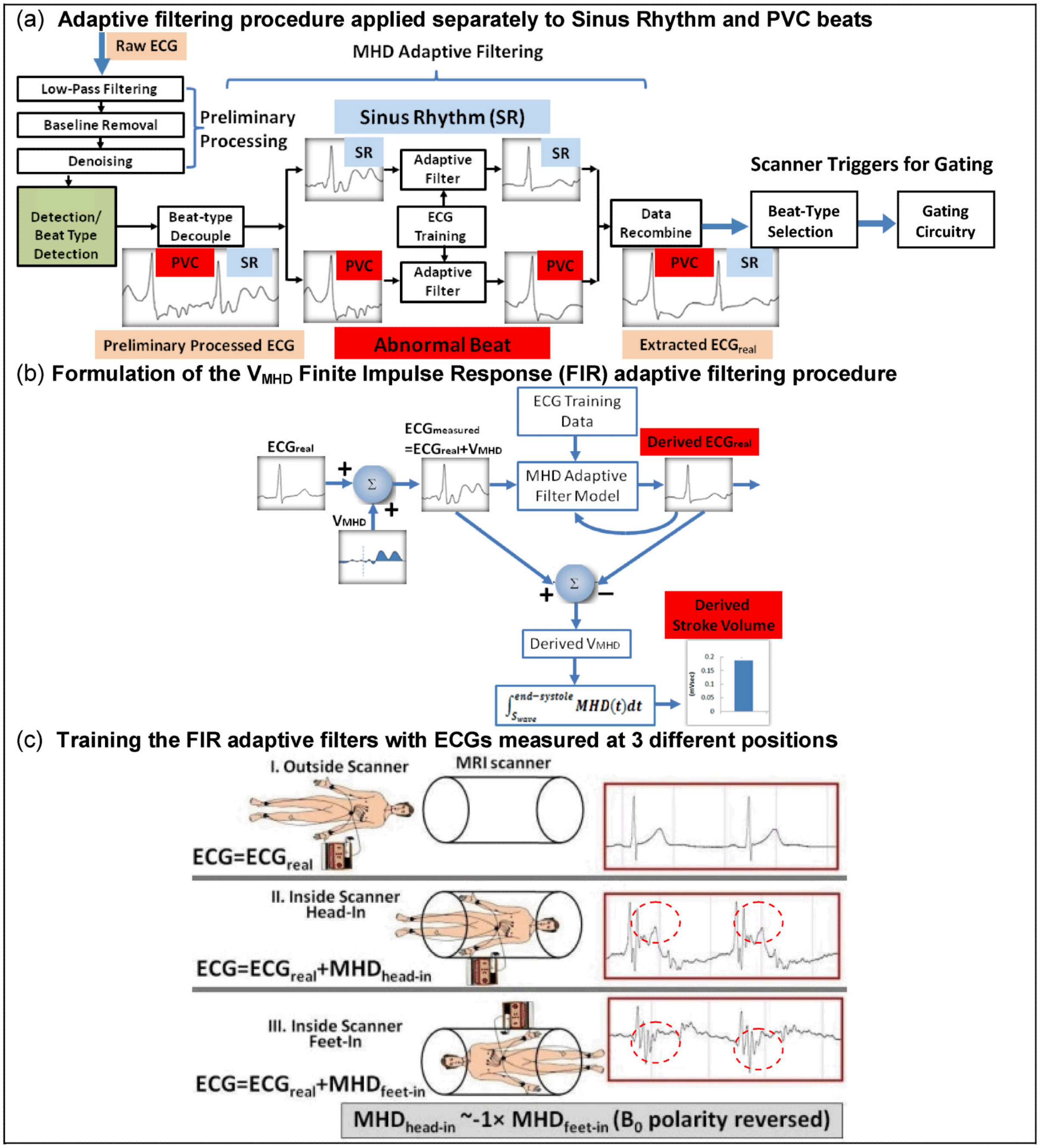

Fig.3.

V$_{MHD}$ filtering procedure: (a) overview and (b) FIR formulation. (c) ECGs measured at three positions for filter training. In positions (ii) and (iii), V$_{MHD}$s (red dotted circles) were superimposed on ECG$_{real}$, with V$_{MHD}$ polarity approximately reversed between (ii) & (iii).

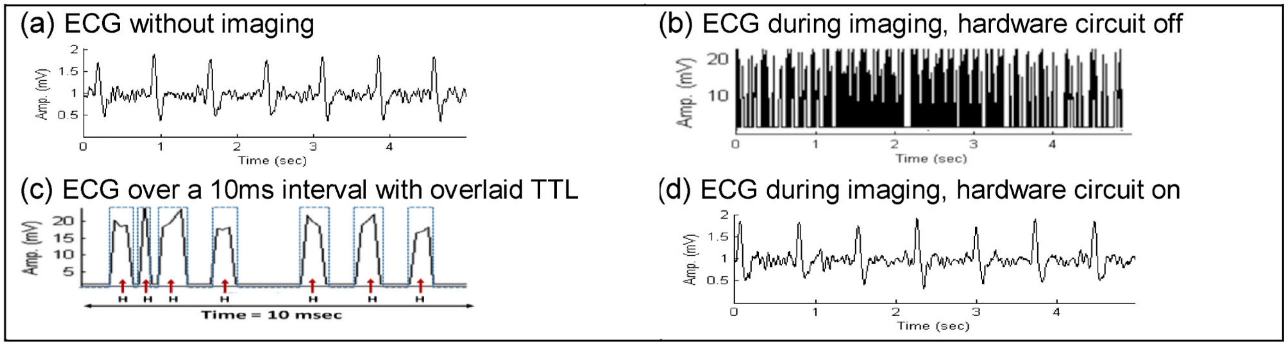

Fig.4.

ECG trace inside a 1.5T scanner (a) without and (b) with imaging. (c) Zoomed time display of (b), showing the corresponding noisy periods, along with the TTL signals (H) received from the detection circuit (dotted lines). Without the GR&RF circuitry, strong noise significantly distorted the ECG. (d) ECG during imaging, with the switching circuitry blocking the GR&RF noise.

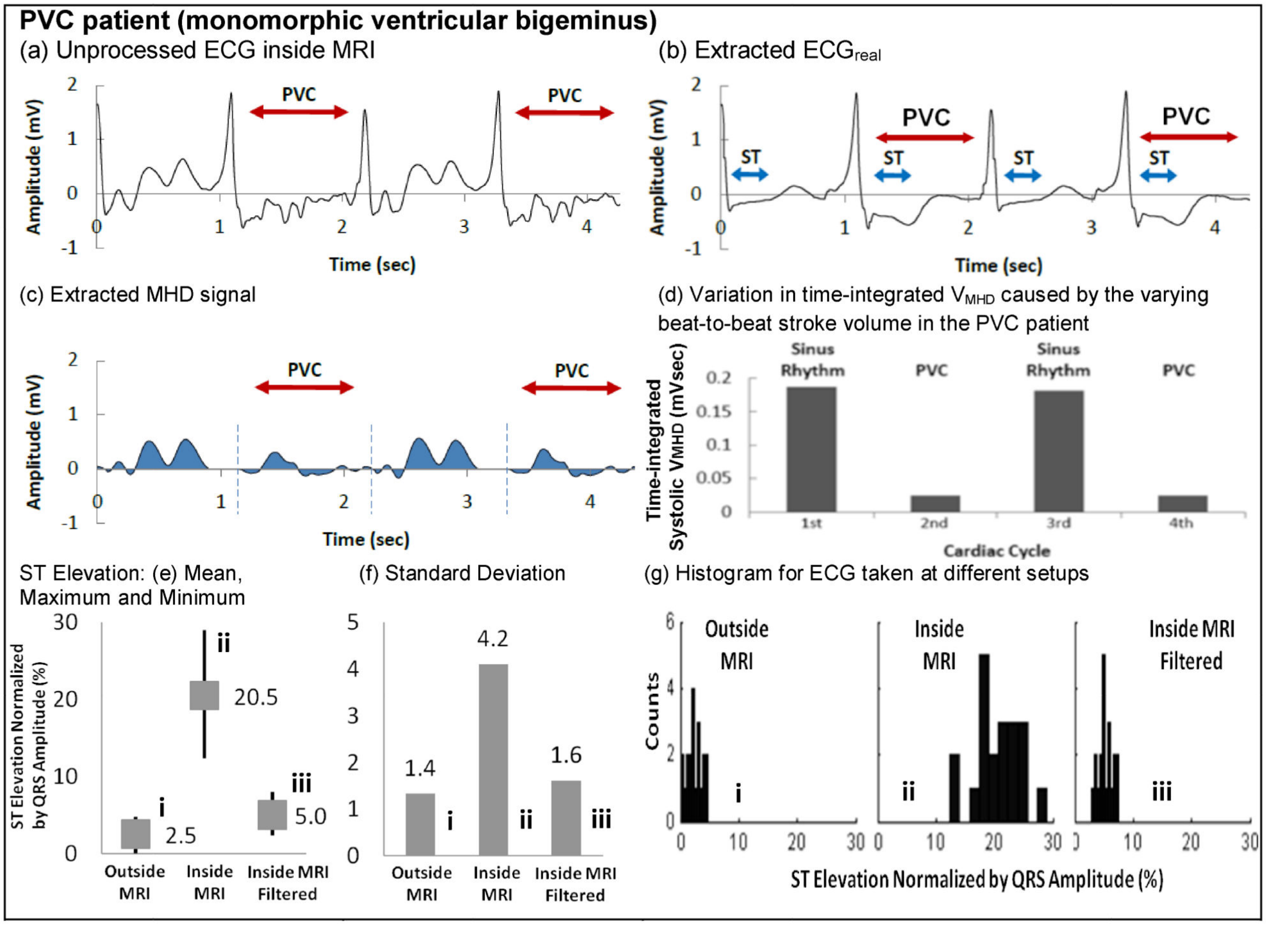

Fig.5.

ECG processing examples of (a-d) PVC patient#1 with monomorphic ventricular bigeminus. (e) Mean, (f) standard deviations and (g) histograms of ST segment elevation for ECG (i) taken outside the MRI, (ii) inside the MRI, and (iii) inside the MRI with filtering (ECG_{real}). The ST segment elevation is normalized by the corresponding QRS complex. In (e), average normalized ST segment elevation is 2.5% (equivalent to 0.062mV) for (i), 20.5% (equivalent to 0.513mV) for (ii), and 5% (equivalent to 0.13mV) for (iii). ST segment was significantly elevated from an average of 2.5% to 20.5% between (i) and (ii), and was preserved in (iii) in an average of 5% (increase in 2.5%). (f) is the standard deviations of the normalized ST segment elevation. (ii) has the highest standard deviation because ST segment was masked severely by V_{MHD} subject to the varying blood flow in each cardiac cycle. The standard deviation of situations (i) and (iii) are close, showing that the filtered ECG taken in (iii) is very close to the true ECG in (i). V_{MHD} in (iii) was effectively removed, extracting ECG_{real}. (g) is the histograms in (i), (ii) and (iii), showing the similar data distributions between (i) and (iii), than (ii). Both (i) and (iii) have narrower range in X axis (upper and lower range of the ST elevation), when compared to (ii). The broader range in X axis in (ii) can be explained by the varying V_{MHD} masked in the ECG signals, effectively widening the upper and lower range of ST elevation data.

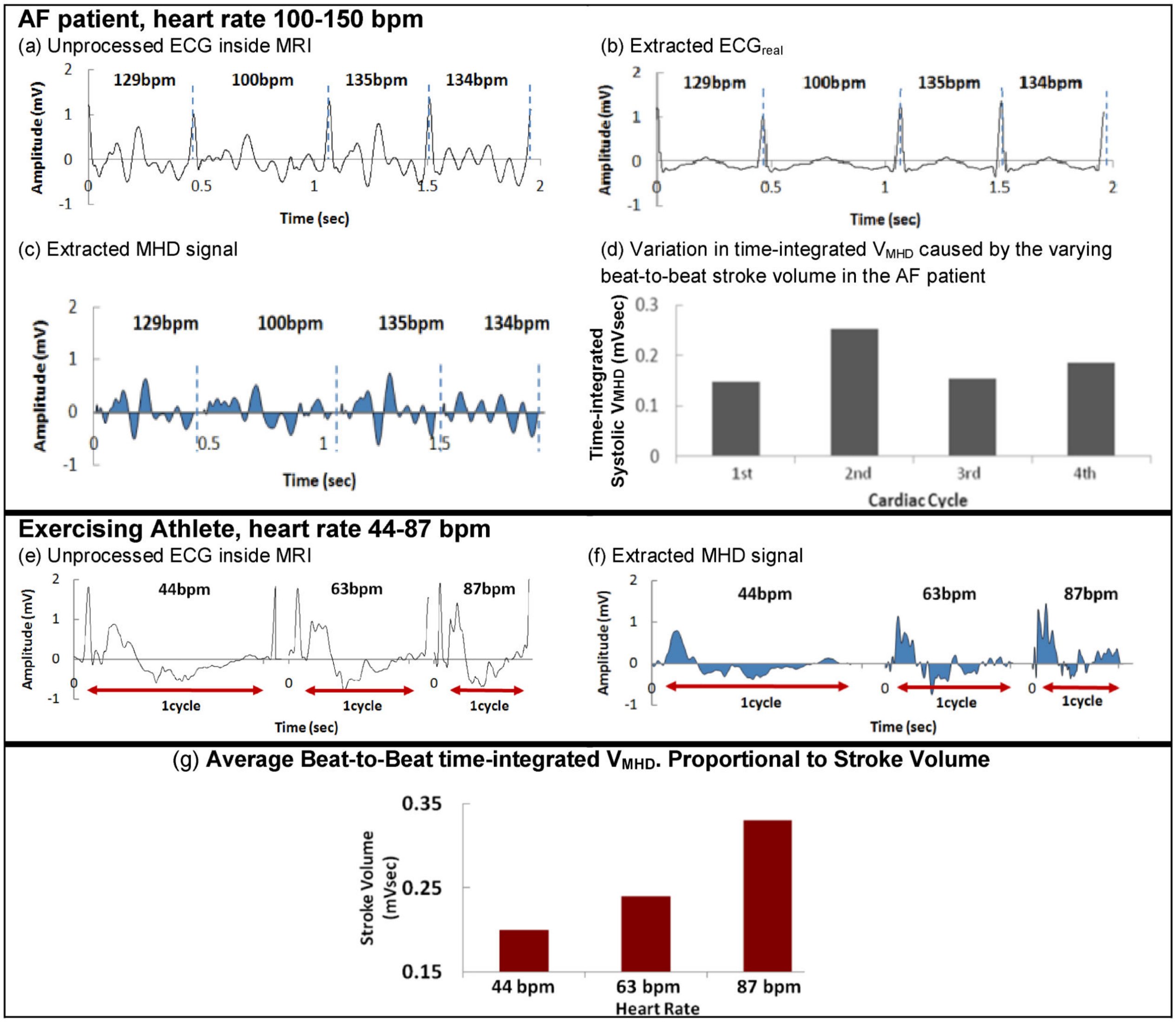

Fig. 6.

ECG processing examples of (a-d) AF patient#1 and (e-g) exercising athlete.

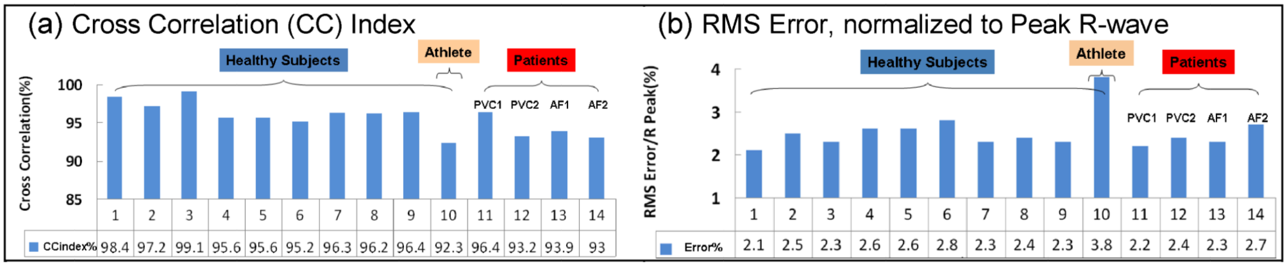

Fig.7.

Validation of MHD filtering accuracy. (a) Cross correlation index and (b) RMS error, normalized by the R-wave peak value, between the processed ECG_{real} and the respective ECG traces acquired outside the MRI.

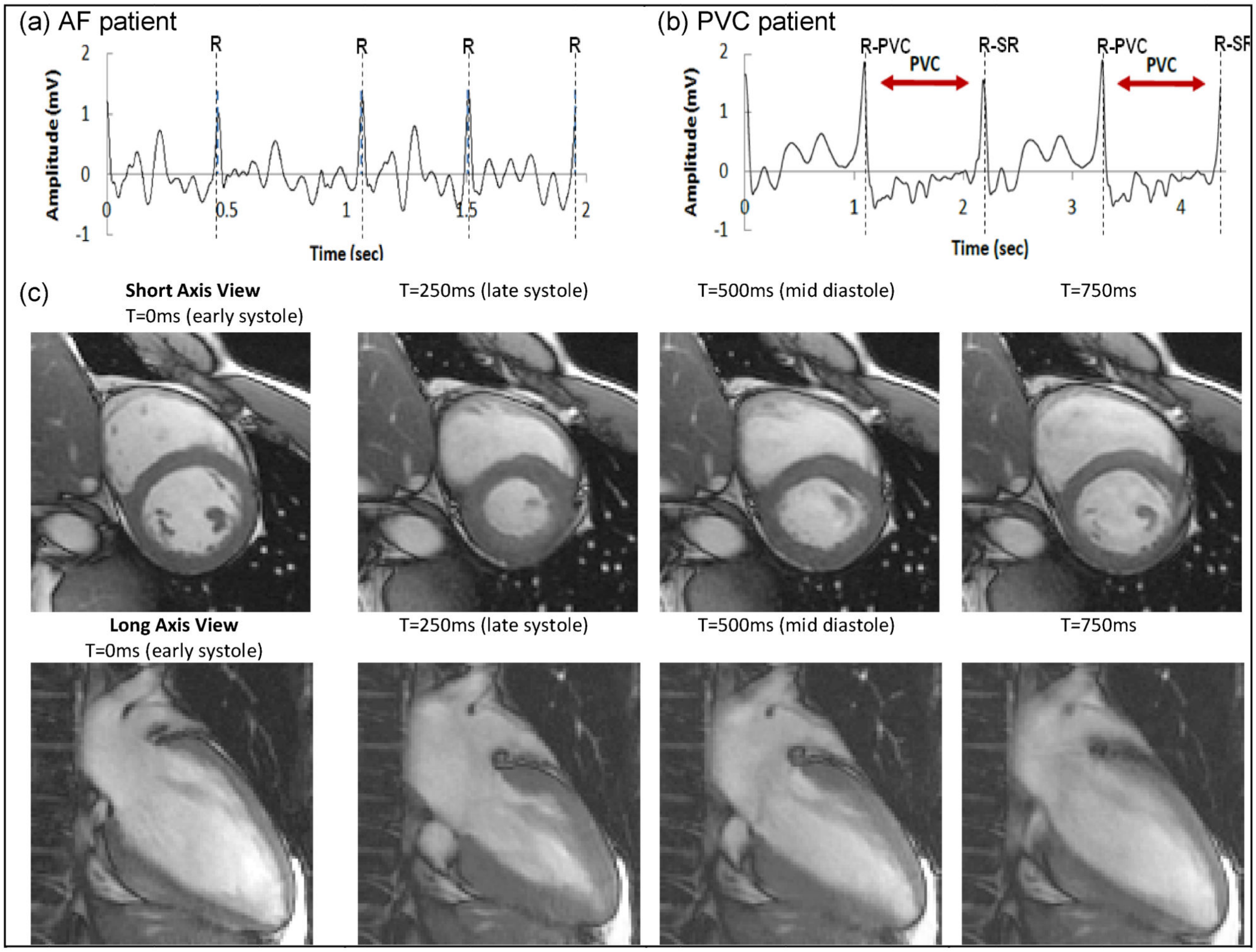

Fig.8.

Intra-MRI ECGs for (a) AF and (b) PVC. R designates detected R-wave peaks for MRI gating. All R peaks (dotted lines) were correctly identified and confirmed by two cardiologists. (c) 12-lead ECG-gated cardiac cine obtained in a subject in which conventional 4-lead ECG failed due to peak MHD voltage.

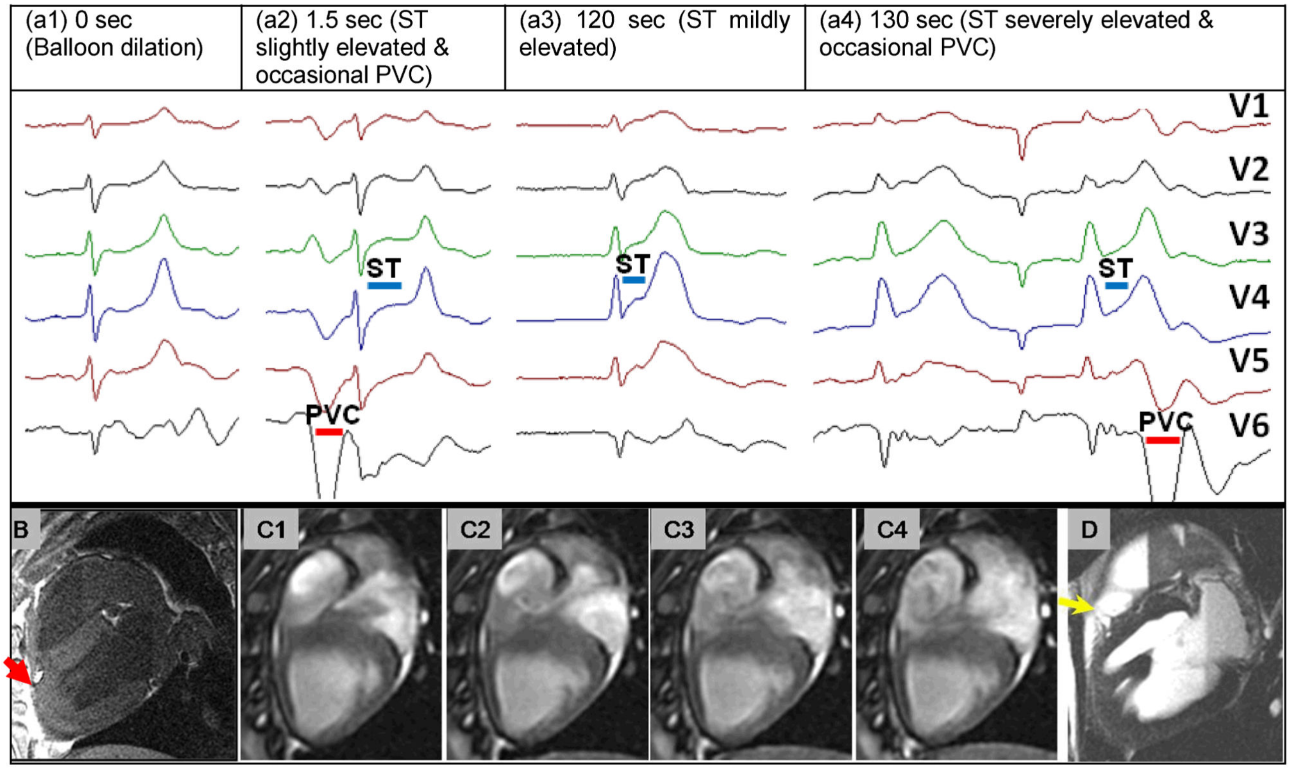

Fig 9.

(a) 12-lead ECG traces acquired inside the MRI at various times after acute-infarction: a1: during LAD balloon dilation (Δt=0 sec), a2: Δt=1.5 sec, a3: Δt=120 sec, a4: Δt=130 sec. Evolution of ST elevation over time (blue line). Occasional PVCs and development of bradycardia are clear. (b) 3D post-mortem T1 image showing position of inflated balloon (red arrow). (c1-4) four cardiac phases from a cine scan showing irregular flow patterns in the right ventricle during ischemia progression at Δt=120-140sec. (d) Post-mortem T2 image showing epicardial edema proximal to occlusion point (yellow arrow).

Table 1

Comparison between computed ECGreal traces and respective traces outside MRI

Comparison between the computed ECGreals and measured ECGs outside the scanner. Measures include the normalized cross-correlation index (CC) and the RMS-error of the fit for four patients, nine non-exercising and one exercising volunteer.

	Healthy Subjects	**Patients**	**Athlete**
CC index	96.2%	94.5%	92.3%
RMS error/R Peak	2.6%	2.3%	3.8%